Supporting Information

Biodegradable π-Conjugated Oligomer Nanoparticles with High Photothermal Conversion Efficiency for Cancer Theranostics

Xiaozhen Li,[†,||] Lu Liu,[‡,||] Shengliang Li,[,†] Yingpeng Wan,[†] Jia-Xiong Chen,[†,#] Shuang Tian,[†] Zhongming Huang,[†] Ya-Fang Xiao,[†] Xiao Cui,[†] Chengyang Xiang,[§] Qinglong Tan,[§] Xiao-Hong Zhang,[#] Weisheng Guo,[*,§] Xing-Jie Liang,[‡] and Chun-Sing Lee[*,†]*

[†]Center of Super-Diamond and Advanced Films (COSDAF), Department of Chemistry, City University of Hong Kong, 83 Tat Chee Avenue, Kowloon, Hong Kong 999077, PR China

[‡]Chinese Academy of Sciences (CAS) Key Laboratory for Biomedical Effects of Nanomaterials and Nanosafety, CAS Center for Excellence in Nanoscience, National Center for Nanoscience and Technology of China, No. 11, First North Road, Zhongguancun, Beijing 100190, P.R China

[§]Translational Medicine Center, State Key Laboratory of Respiratory Disease, The Second Affiliated Hospital, Guangzhou Medical University, Guangzhou 510260, P. R. China

[#]Jiangsu Key Laboratory for Carbon-Based Functional Materials & Devices, Institute of Functional Nano & Soft Materials (FUNSOM), Joint International Research Laboratory of Carbon-Based Functional Materials and Devices, Soochow University, 199 Ren'ai Road, Suzhou 215123, Jiangsu, P.R. China

[*]Address correspondence to:

E-mail: lishengliang@iccas.ac.cn

E-mail: tjuguoweisheng@126.com

E-mail: apcslee@cityu.edu.hk

1. Supporting Figures

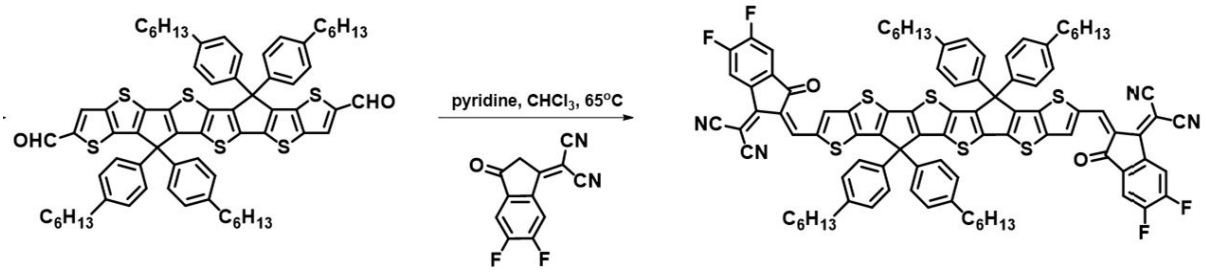

Figure S1. The synthetic route of F8-IC.

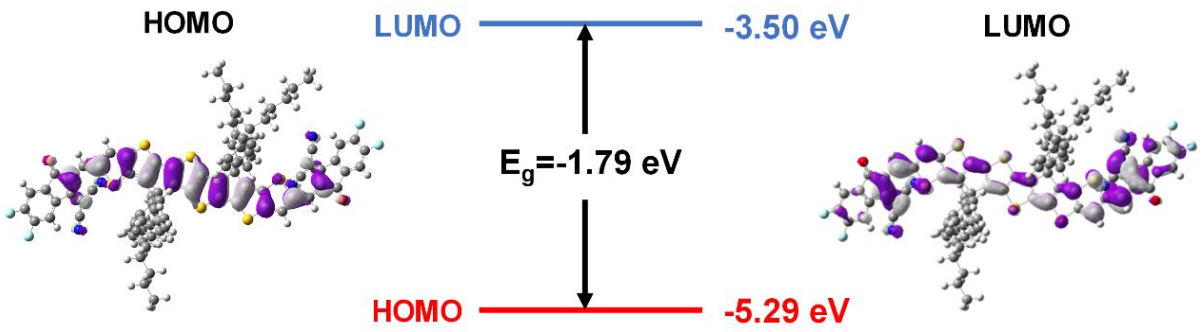

Figure S2. Calculated HOMO and LUMO energy levels of F8-IC.

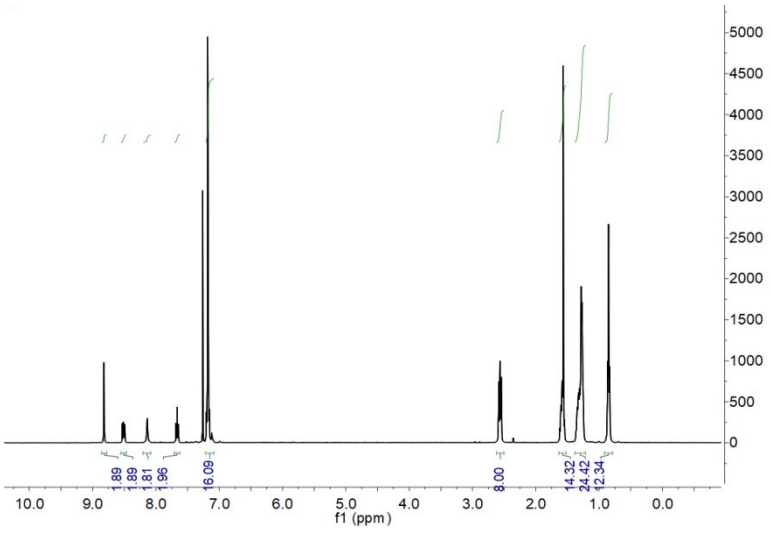

Figure S3. ^{1}H NMR spectrum of F8-IC in $CDCl_3$.

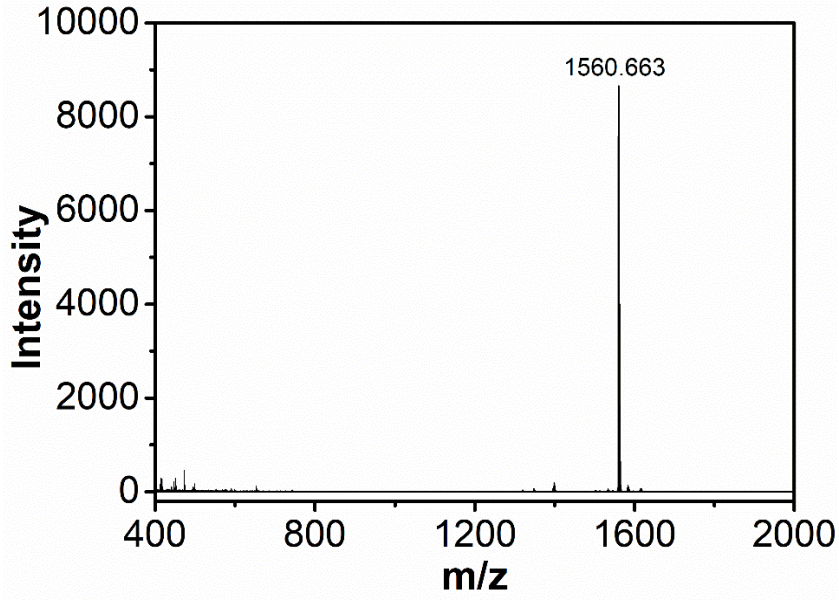

Figure S4. The Matrix assisted laser desorption/ionization time-of-flight (MALDI-TOF) mass spectrum of F8-IC.

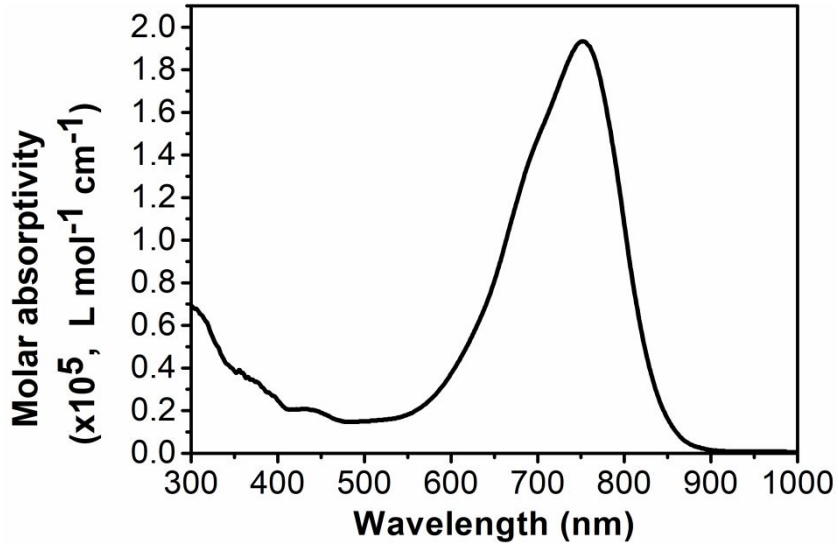

Figure S5. Molar absorptivity of F8-IC (6.25 μg mL^{-1}) in THF against the wavelength.

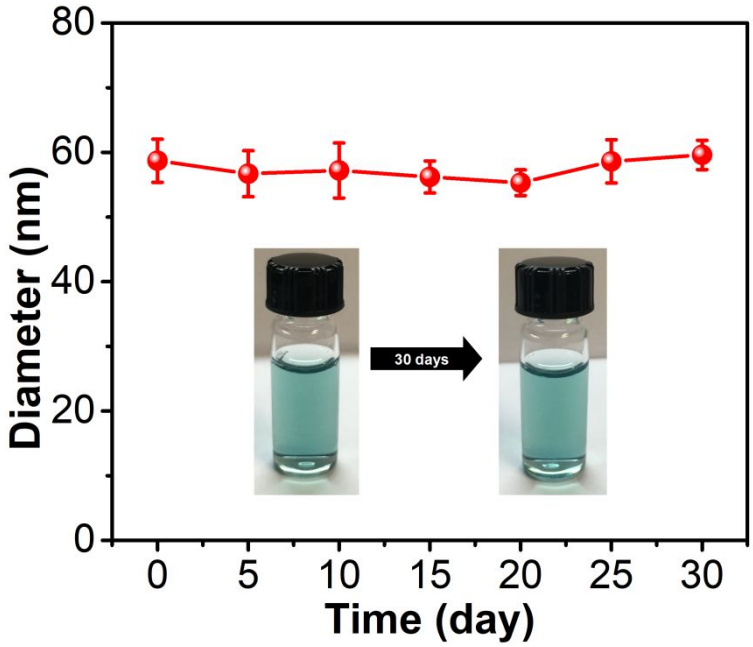

Figure S6 Size stability of F8-PEG NPs during 30-day storage, insets are corresponding photographs of the F8-PEG NPs dispersions after 30-day storage.

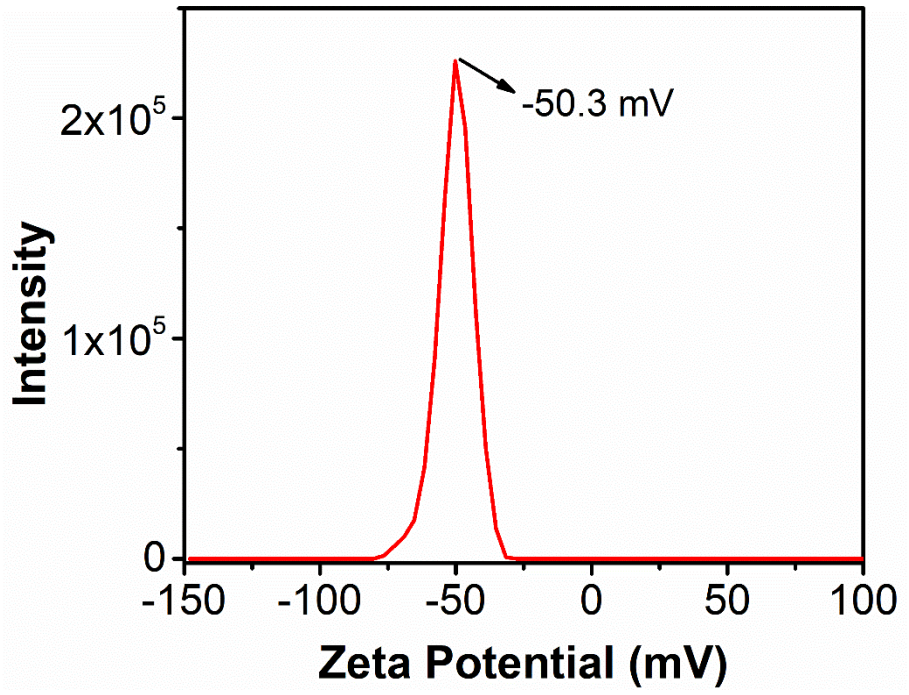

Figure S7. Zeta potential of F8-PEG NPs in DI water.

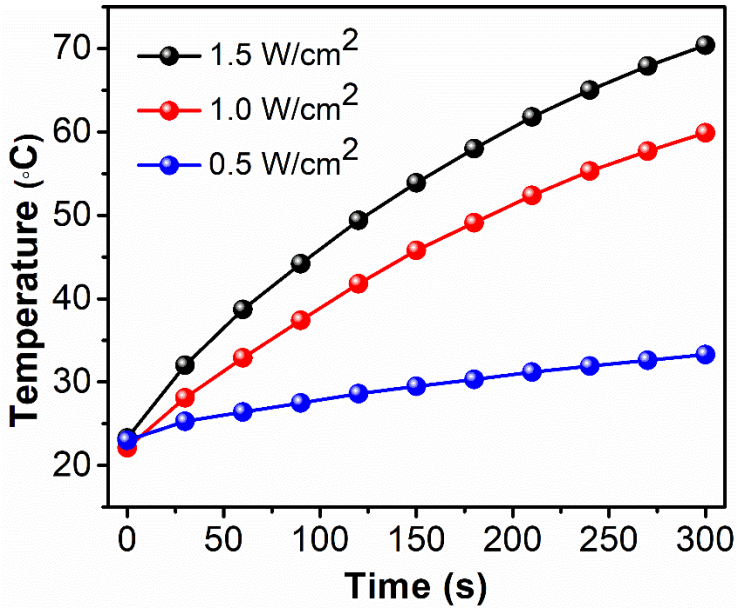

Figure S8. Photothermal heating curves of a F8-PEG NP water dispersion (50 μg mL^{-1}) under different laser power densities as a function of time.

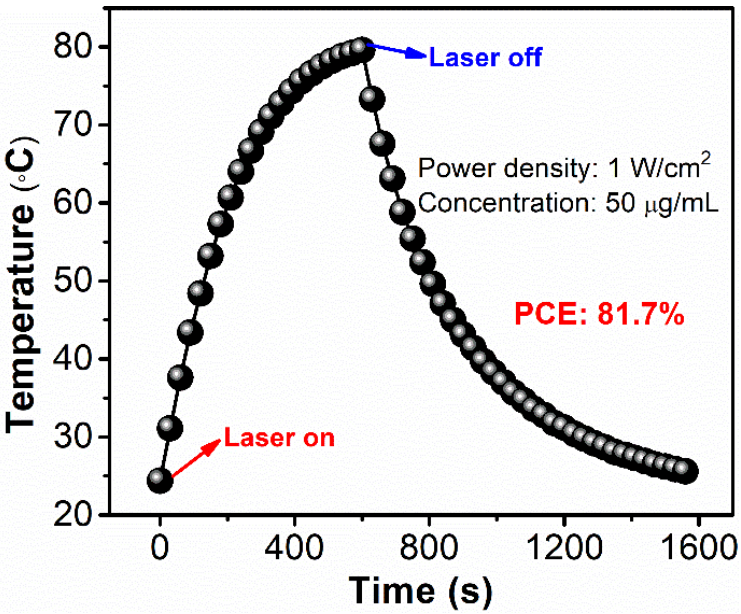

Figure S9. Photothermal effect of S6F4N aqueous solution upon laser irradiation (1W/cm^2) which was turned off after irradiation for 10 minutes.

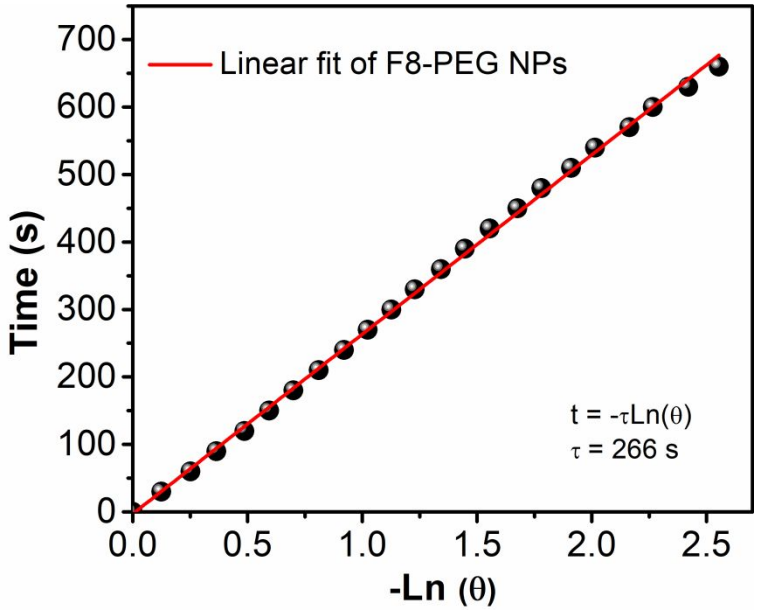

Figure S10. Plot of cooling time vs. negative natural logarithm of the temperature change obtained from the cooling stage as displayed in Figure S8.

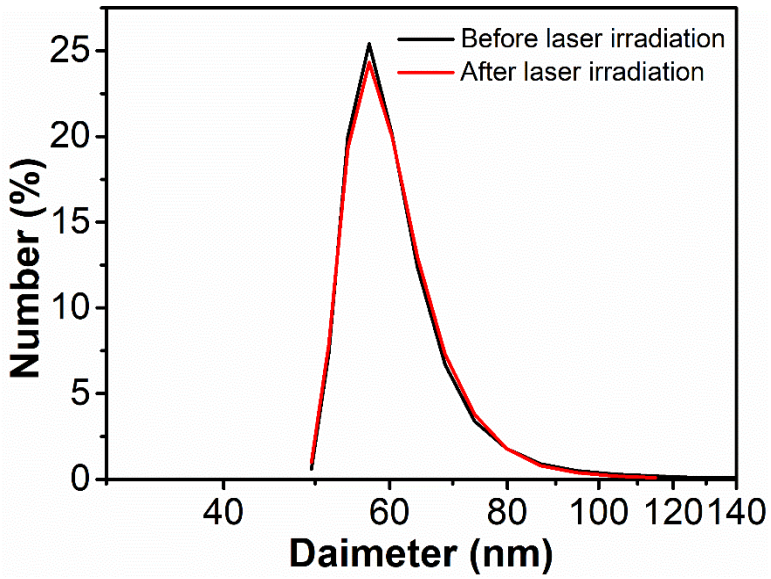

Figure S11. DLS profile of F8-PEG NPs before and after laser irradiation.

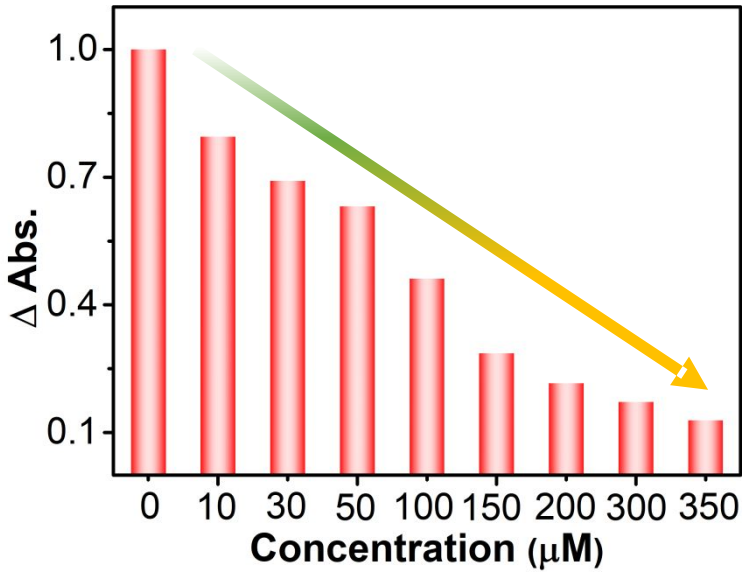

Figure S12. Absorption decrease rate of F8-IC (2 μg/mL) at 750 nm after titration with HClO with different concentrations.

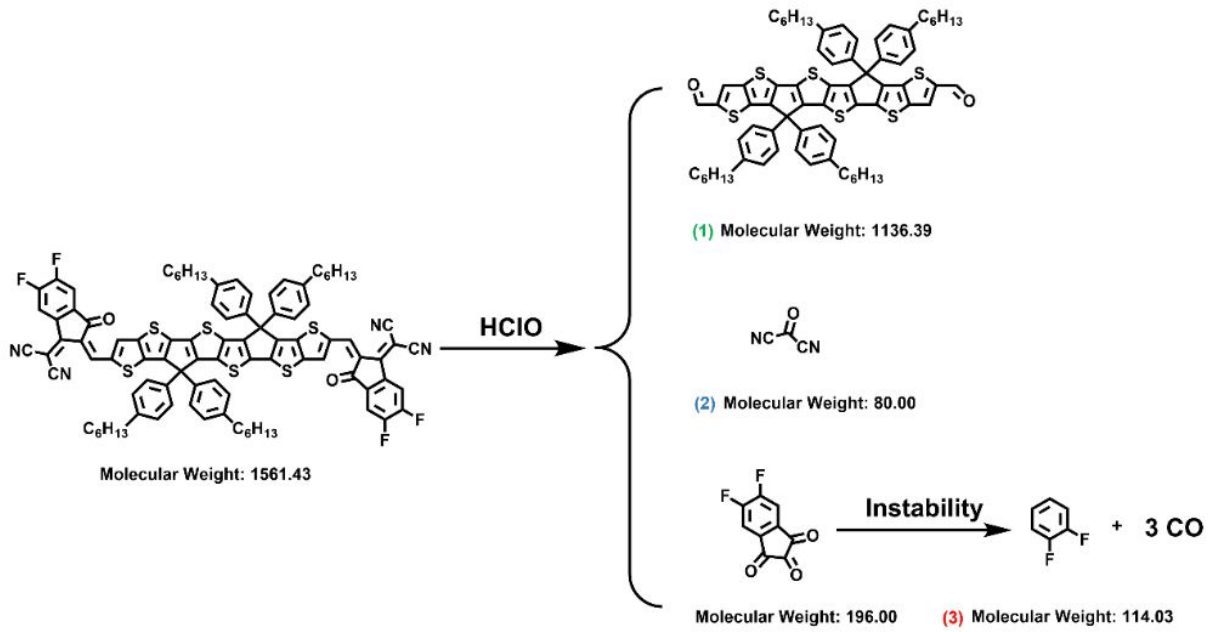

Figure S13. Possible reaction mechanism between F8-IC and HClO.

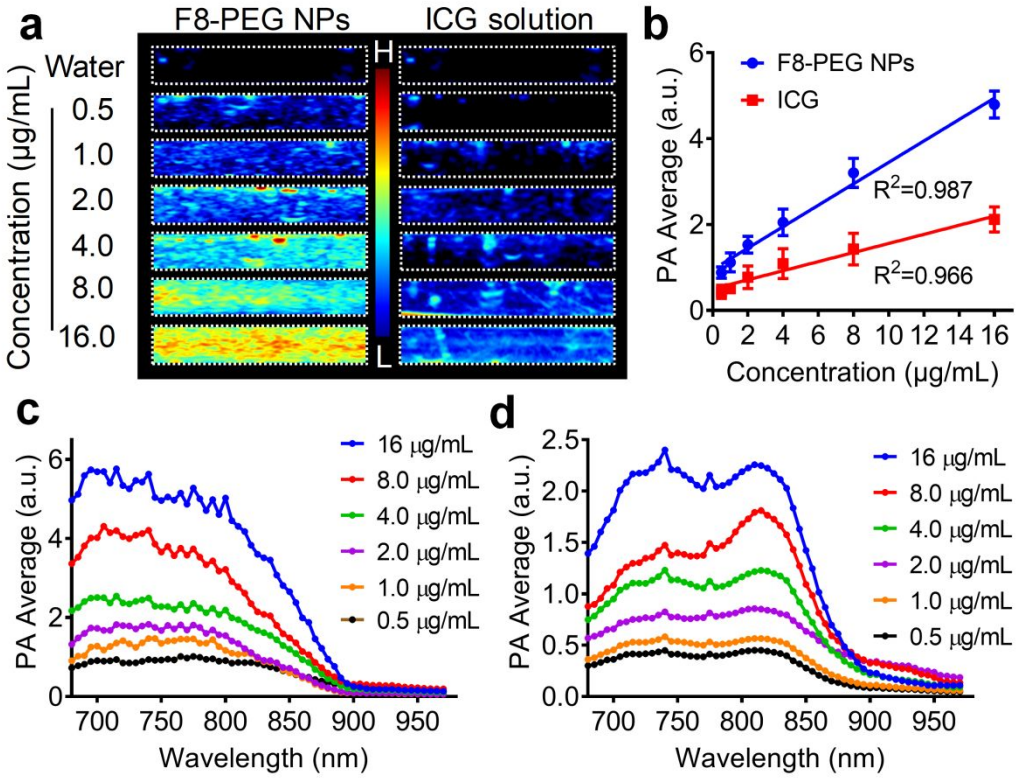

Figure S14. a) Phantom tests of F8-PEG NPs and ICG solution with different concentrations. b) PA quantification of the phantom tests. c) PA spectra of F8-PEG NPs, and d) ICG solution with different concentrations under full-wavelength excitation (680-970 nm). The scanning interval is 5 min. These data were acquired from Vero LAZR system (FUJIFILM VisualSonics, Toronto, Canada), and processed using Vero Lab software.

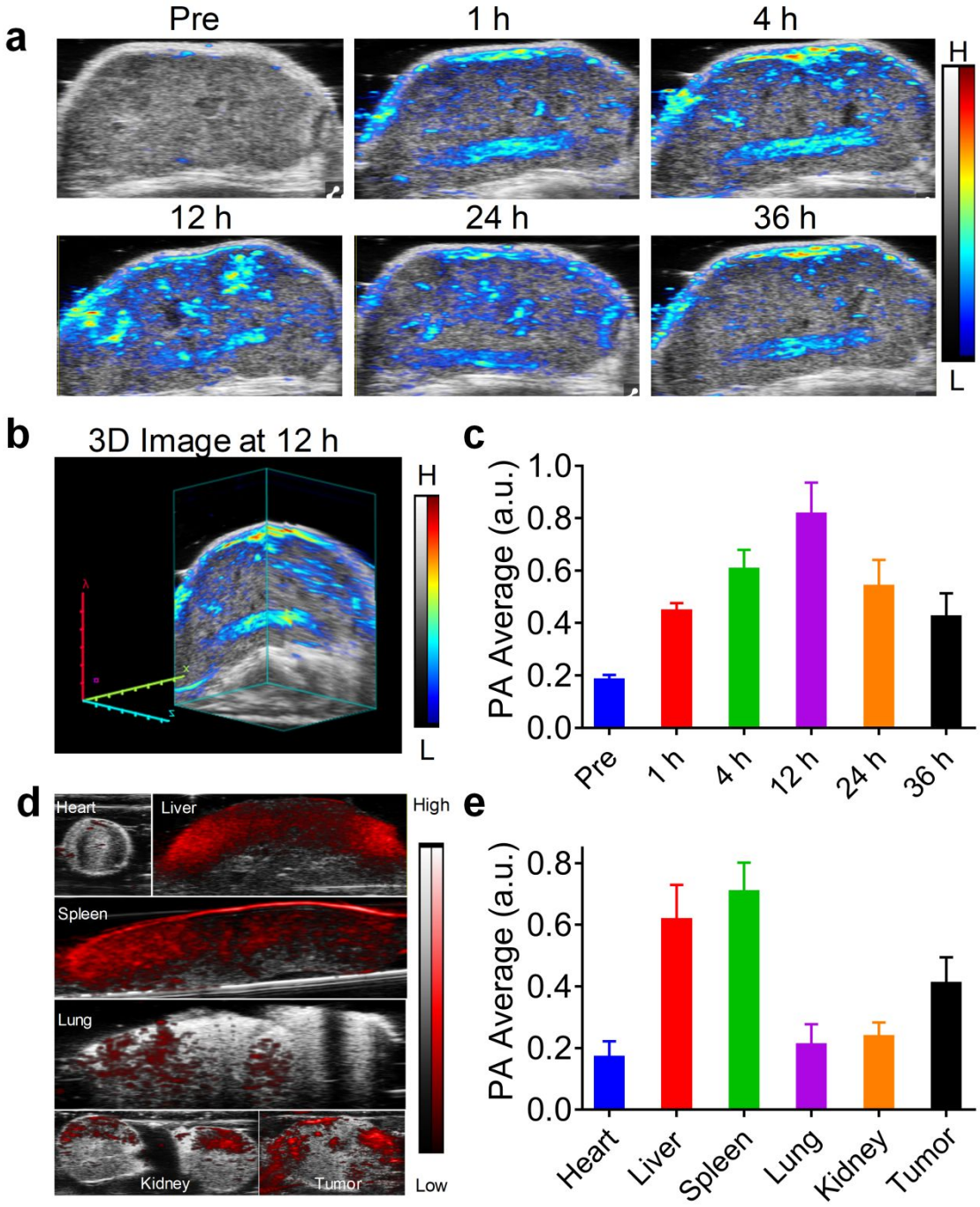

Figure S15. a) *In vivo* PA imaging of tumor at different post-injection time points (0, 1, 4, 12, 24, and 36 h). b) Three dimensional images at 12h. c) The PA intensity quantification of tumor site at different post-injection time points. d) The PA imaging of heart, liver, spleen, lung, kidney, and tumor dissected from mice after 36 h injection of F8-PEG NPs. e) The PA intensity quantification of the indicated

tissues. These data were acquired from Vero LAZR system (FUJIFILM VisualSonics, Toronto, Canada), and processed using Vero Lab software.

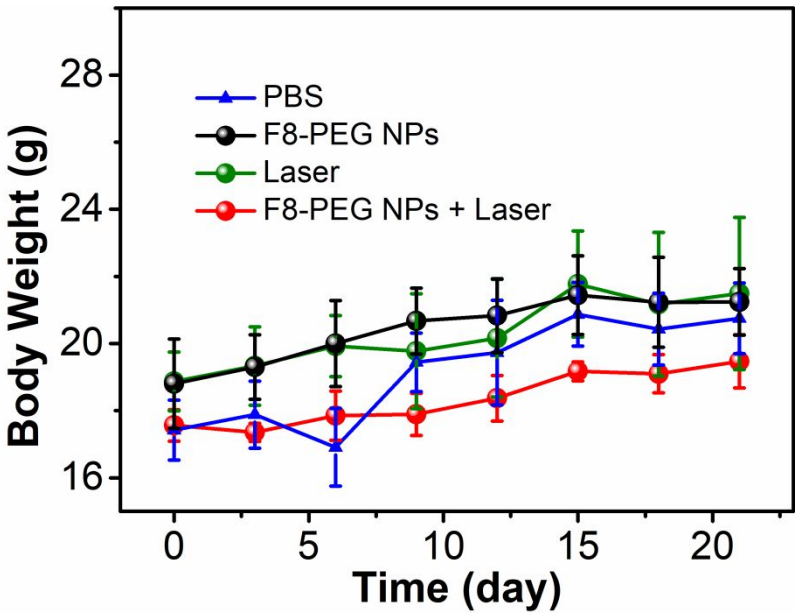

Figure S16. Bodyweight changes of mice in different groups.

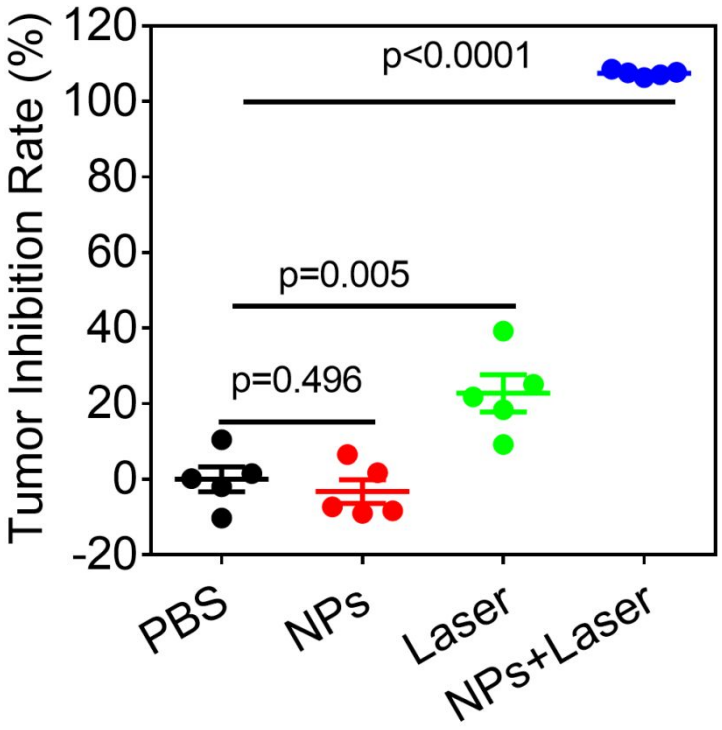

Figure S17. *Tumor suppression efficacy of different treatments.*

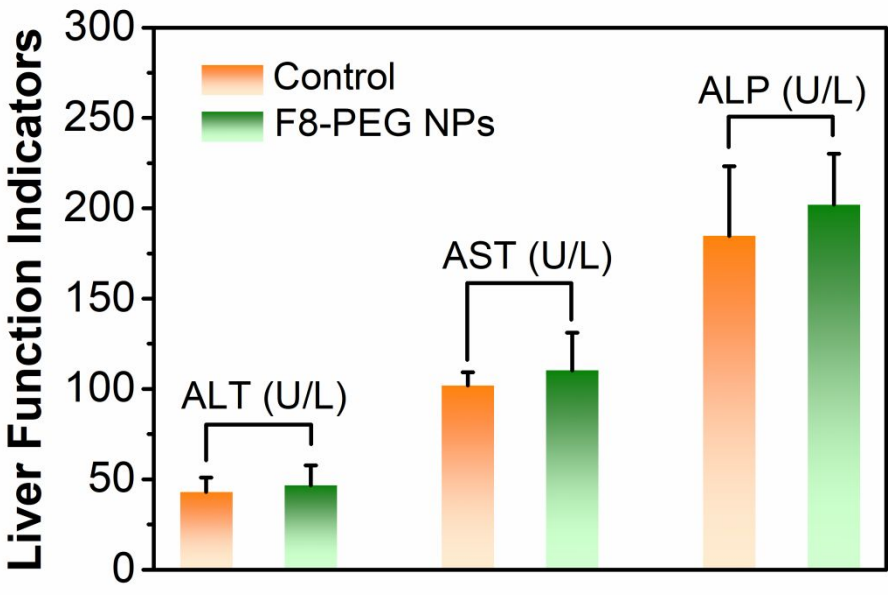

Figure S18. Biochemical analysis of liver for the PBS- and F8-PEG NPs + laser-treated mice. The markers include alanine transaminase (ALT), aspartate transaminase (AST) and Alkaline Phosphatase (ALP).

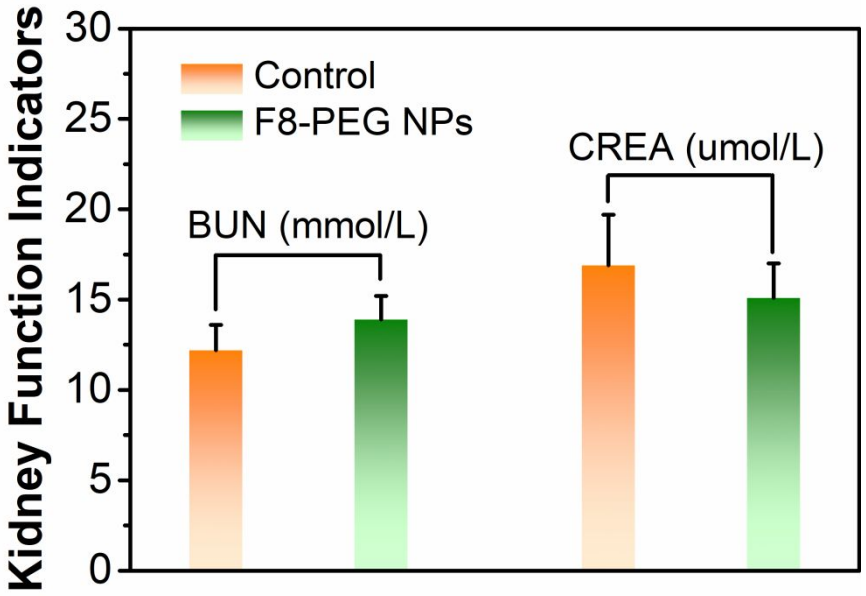

Figure S19. Biochemical analysis of kidney for the PBS- and F8-PEG NPs + laser-treated mice. The markers include blood urea nitrogen (BUN) and creatinine (CREA).

Table S1 Summary of photothermal conversion efficiencies (PCEs) of recently reported state-of-the-art photothermal agents

Categories	Photothermal agents	Laser irradiation (nm)	PCE (%)	Ref.
Conjugated oligomers	**F8-PEG NPs**	**808**	**82**	**this work**
	N4 NPs	808	**30**	[1]
	DPP-TPA	660	**34.5**	[2]
	2TPE-NDTA-doped NPs	808	**54.9**	[3]
Conjugated polymers	Pdots	808	**65**	[4]
	SPN1	655	**52.6**	[5]
	PPor-PEG NPs	635	**62.3**	[6]
	DSPN	808	**30.8**	[7]
	CP-NPs	785	**34.7**	[8]
	PPy NPs	808	**44.7**	[9]
Small molecular dyes	ICG	780	**15.1**	[10]
	TPC-SS NPs	635	**37**	[11]
	Mito-CCy	730	**9.5**	[12]
	IABDP NPs	730	**37.9**	[13]
	IRPDA@PFH NDs	808	**57.7**	[14]
Inorganic materials	Gold bellflowers	808	**74**	[15]
	Gold nanocage	808	**63**	[16]
	$Cu–Ag_2S$/PVP nanoparticles	808	**58.2**	[17]
	MoS_2 radar-like nanoparticles	808	**53.3**	[18]

Table S2 Comparison of mass extinction coefficient (ε) of F8-PEG NPs with reported PTT agents

PTT agents	Wavelength (nm)	ε (cm^{-1} g^{-1} L)	Ref.
F8-PEG NPs	750	**123.4**	this work
Pdots	808	**72.9**	[4]
SPN4	748	**76**	[19]
SPN1	655	**34.9**	[5]
CP-NPs	785	**7.2**	[8]
PorCP NPs	800	**34.68**	[20]
ICG	780	**191**	[12]
Mito-CCy	713	**112.2**	[12]
Cyanine dye (RC)	868	**120.1**	[21]
gold nanorods	808	**3.9**	[22]
BPQDS	808	**14.8**	[22]
graphene oxide	808	**3.6**	[23]

2. Synthesis of F8-IC

F8-IC was synthesized *via* Knoevenagel condensation reaction according to the previously reported method (Supporting information).[24] Briefly, 6,6,12,12-tetrakis(4-hexylphenyl)-6,12-dihydro-Thieno[2",3":4',5']thieno[3',2':4,5]cyc -lopenta[1,2-b]thieno[2"',3"':4",5"]thieno[2",3":3',4']cyclopenta[1',2':4,5]thieno[2,3-d]thiophene-2,8-dicarboxaldehyde (57 mg, 0.05 mmol) and 2-(5,6-Difluoro-3-oxo-2,3-dihydro-1H-inden-1-ylidene)malononitrile (46 mg, 0.05 mmol) were dissolved in the dry chloroform ($CHCl_3$, 20 mL) and then added into a two-neck flask (50 mL). Then pyridine (0.5 mL) was added into the above flask and flushed with nitrogen. Under reflux condenser, the mixture was vigorously stirred at 65 ℃ for 1 day and then cooled to room temperature, 100 mL CH_3OH was used to precipitate the resultant, and then filtered for purification using column chromatography on silica gel, and then vacuum drying gave a dark green solid (46.4 mg, 45%).

3. Calculation of Photothermal conversion efficiency

The photothermal conversion efficiency was calculated according to the reported method.[6] Specifically, photothermal conversion efficiency (η) of F8-PEG NPs was calculated by monitoring temperature change of F8-PEG NPs in aqueous dispersion (50 μg mL^{-1}) as a function of time under continuous laser irradiation (808 nm, 1W cm^{-2}) for 10 min (t). When the temperature reached to a plateau, the laser was turned off and the temperature was recorded during the cooling stage until the temperature decreased to the room temperature. η was determined according to Equation (a):

$$\eta = \frac{hA\,(T_{Max} - T_{Surr}) - Q_{Dis}}{I\,(1 - 10^{-A808})} \qquad \text{(a)};$$

where η denotes the heat transfer coefficient, A is the surface area of the container, T_{Max} and T_{Surr} are the plateau temperature and ambient temperature of the surroundings, respectively. Q_{Dis} represents the

heat dissipation from the light absorbed by the solvent and the quartz sample cell, I is the incident laser power, and A_{808} is the absorbance of the sample at 808 nm. The value of hA is obtained from Equation (b):

$$\tau_S = \frac{m_D c_D}{hA} \quad \text{(b);}$$

where, m_D and c_D represent the mass (1.0 g) and heat capacity (4.2 J g^{-1}), respectively of DI water used to disperse the F8-PEG NPs. τ_s is the time constant for heat transfer of the system, which is calculated from Equation (c):

$$t = -\tau_S \ln(\theta) = -\tau_S \ln\left(\frac{T_t - T_{Surr}}{T_{Max} - T_{Surr}}\right) \quad \text{(c);}$$

where, t is the cooling time points after continuous irradiation for 10 mins, T_t is the corresponding temperature of F8-PEG NPs during the cooling stage, and according to Figure S9, τ_s is calculated to be 266 s. Based on Equation (b) and (c), the value of hA is determined to be 0.016 W. Q_{Dis} represents the heat dissipation from the light absorbed by the water and the container, which is determined according to Equation (d).

$$Q_{Dis} = \frac{c_D m_D (T_{Max(water)} - T_{Surr})}{\tau_{S(water)}} \quad \text{(d)}$$

Where, T_{Max} (water) is 24.8 °C and τ_{water} is 275 s, thus Q_{Dis} was determined to be 0.0504. According to the experiment data and Equation (1), η was calculated to be 82%.

4) The tumor growth inhibition efficiency was calculated based on the following equation:

$$r = \left(1 - \frac{V'_f - V'_0}{V_f - V_0}\right) \times 100\%$$

where V_f and V_0 represent the final and initial tumor volume of the saline group, while V'_f and V'_0 represent the final and initial tumor volume of the treatment group.

References

(1) Cai, X.; Liu, X.; Liao, L. D.; Bandla, A.; Ling, J. M.; Liu, Y. H.; Thakor, N.; Bazan, G. C.; Liu, B., Encapsulated Conjugated Oligomer Nanoparticles for Real-Time Photoacoustic Sentinel Lymph Node Imaging and Targeted Photothermal Therapy. *Small* **2016,** *12*, 4873-4880.

(2) Cai, Y.; Liang, P.; Tang, Q.; Yang, X.; Si, W.; Huang, W.; Zhang, Q.; Dong, X., Diketopyrrolopyrrole–Triphenylamine Organic Nanoparticles as Multifunctional Reagents for Photoacoustic Imaging-Guided Photodynamic/Photothermal Synergistic Tumor Therapy. *ACS Nano* **2017,** *11*, 1054-1063.

(3) Zhao, Z.; Chen, C.; Wu, W.; Wang, F.; Du, L.; Zhang, X.; Xiong, Y.; He, X.; Cai, Y.; Kwok, R. T. K.; Lam, J. W. Y.; Gao, X.; Sun, P.; Phillips, D. L.; Ding, D.; Tang, B. Z., Highly Efficient Photothermal Nanoagent Achieved by Harvesting Energy *via* Excited-State Intramolecular Motion within Nanoparticles. *Nat. Commun.* **2019,** *10*, 768.

(4) Li, S.; Wang, X.; Hu, R.; Chen, H.; Li, M.; Wang, J.; Wang, Y.; Liu, L.; Lv, F.; Liang, X.-J.; Wang, S., Near-Infrared (NIR)-Absorbing Conjugated Polymer Dots as Highly Effective Photothermal Materials for *In Vivo* Cancer Therapy. *Chem. Mater.* **2016,** *28*, 8669-8675.

(5) Zhang, J.; Chen, J.; Ren, J.; Guo, W.; Li, X.; Chen, R.; Chelora, J.; Cui, X.; Wan, Y.; Liang, X.-J.; Hao, Y.; Lee, C.-S., Biocompatible Semiconducting Polymer Nanoparticles as Robust Photoacoustic and Photothermal Agents Revealing the Effects of Chemical Structure on High Photothermal Conversion Efficiency. *Biomaterials* **2018,** *181*, 92-102.

(6) Zhang, J.; Yang, C.; Zhang, R.; Chen, R.; Zhang, Z.; Zhang, W.; Peng, S.-H.; Chen, X.; Liu, G.; Hsu, C.-S.; Lee, C.-S., Biocompatible D–A Semiconducting Polymer Nanoparticle with Light-

Harvesting Unit for Highly Effective Photoacoustic Imaging Guided Photothermal Therapy. *Adv. Funct. Mater.* **2017,** *27*, 1605094.

(7) Jiang, Y.; Cui, D.; Fang, Y.; Zhen, X.; Upputuri, P. K.; Pramanik, M.; Ding, D.; Pu, K., Amphiphilic Semiconducting Polymer as Multifunctional Nanocarrier for Fluorescence/Photoacoustic Imaging Guided Chemo-Photothermal Therapy. *Biomaterials* **2017,** *145*, 168-177.

(8) Yang, T.; Liu, L.; Deng, Y.; Guo, Z.; Zhang, G.; Ge, Z.; Ke, H.; Chen, H., Ultrastable Near-Infrared Conjugated-Polymer Nanoparticles for Dually Photoactive Tumor Inhibition. *Adv. Mater.* **2017,** *29*, 1700487.

(9) Chen, M.; Fang, X.; Tang, S.; Zheng, N., Polypyrrole Nanoparticles for High-Performance *In Vivo* Near-Infrared Photothermal Cancer Therapy. *Chem. Commun.* **2012,** *48*, 8934-8936.

(10) Zheng, M.; Zhao, P.; Luo, Z.; Gong, P.; Zheng, C.; Zhang, P.; Yue, C.; Gao, D.; Ma, Y.; Cai, L., Robust ICG Theranostic Nanoparticles for Folate Targeted Cancer Imaging and Highly Effective Photothermal Therapy. *ACS Appl. Mater. Interfaces* **2014,** *6*, 6709-6716.

(11) Zheng, X.; Wang, L.; Liu, S.; Zhang, W.; Liu, F.; Xie, Z., Nanoparticles of Chlorin Dimer with Enhanced Absorbance for Photoacoustic Imaging and Phototherapy. *Adv. Funct. Mater.* **2018,** *28*, 1706507.

(12) Jung, H. S.; Lee, J.-H.; Kim, K.; Koo, S.; Verwilst, P.; Sessler, J. L.; Kang, C.; Kim, J. S., A Mitochondria-Targeted Cryptocyanine-Based Photothermogenic Photosensitizer. *J. Am. Chem. Soc.* **2017,** *139*, 9972-9978.

(13) Tang, Q.; Si, W.; Huang, C.; Ding, K.; Huang, W.; Chen, P.; Zhang, Q.; Dong, X., An Aza-BODIPY Photosensitizer for Photoacoustic and Photothermal Imaging Guided Dual Modal Cancer Phototherapy. *J. Mat. Chem. B* **2017,** *5*, 1566-1573.

(14) Zhu, H.; Qin, D.; Wu, Y.; Jing, B.; Liu, J.; Hazlewood, D.; Zhang, H.; Feng, Y.; Yang, X.; Wan, M.; Wu, D., Laser-Activated Bioprobes with High Photothermal Conversion Efficiency for Sensitive Photoacoustic/Ultrasound Imaging and Photothermal Sensing. *ACS Appl. Mater. Interfaces* **2018,** *10*, 29251-29259.

(15) Huang, P.; Rong, P.; Lin, J.; Li, W.; Yan, X.; Zhang, M. G.; Nie, L.; Niu, G.; Lu, J.; Wang, W.; Chen, X., Triphase Interface Synthesis of Plasmonic Gold Bellflowers as Near-Infrared Light Mediated Acoustic and Thermal Theranostics. *J. Am. Chem. Soc.* **2014,** *136*, 8307-8313.

(16) Zeng, J.; Goldfeld, D.; Xia, Y., A Plasmon-Assisted Optofluidic (PAOF) System for Measuring the Photothermal Conversion Efficiencies of Gold Nanostructures and Controlling an Electrical Switch. *Angew. Chem. Int. Ed. Engl.* **2013,** *52*, 4169-4173.

(17) Dong, L.; Ji, G.; Liu, Y.; Xu, X.; Lei, P.; Du, K.; Song, S.; Feng, J.; Zhang, H., Multifunctional Cu-Ag_2S Nanoparticles with High Photothermal Conversion Efficiency for Photoacoustic Imaging-Guided Photothermal Therapy *In Vivo*. *Nanoscale* **2018,** *10*, 825-831.

(18) Huang, Z.; Qi, Y.; Yu, D.; Zhan, J., Radar-Like MoS_2 Nanoparticles as a Highly Efficient 808 nm Laser-Induced Photothermal Agent for Cancer Therapy. *RSC Adv.* **2016,** *6*, 31031-31036.

(19) Pu, K.; Mei, J.; Jokerst, J. V.; Hong, G.; Antaris, A. L.; Chattopadhyay, N.; Shuhendler, A. J.; Kurosawa, T.; Zhou, Y.; Gambhir, S. S.; Bao, Z.; Rao, J., Diketopyrrolopyrrole-Based Semiconducting Polymer Nanoparticles for *In Vivo* Photoacoustic Imaging. *Adv. Mater.* **2015,** *27*, 5184-5190.

(20) Guo, B.; Feng, G.; Manghnani, P. N.; Cai, X.; Liu, J.; Wu, W.; Xu, S.; Cheng, X.; Teh, C.; Liu, B., A Porphyrin-Based Conjugated Polymer for Highly Efficient *In Vitro* and *In Vivo* Photothermal Therapy. *Small* **2016,** *12*, 6243-6254.

(21) Zhou, B.; Li, Y.; Niu, G.; Lan, M.; Jia, Q.; Liang, Q., Near-Infrared Organic Dye-Based Nanoagent for the Photothermal Therapy of Cancer. *ACS Appl. Mater. Interfaces* **2016,** *8*, 29899-29905.

(22) Sun, Z.; Xie, H.; Tang, S.; Yu, X.-F.; Guo, Z.; Shao, J.; Zhang, H.; Huang, H.; Wang, H.; Chu, P. K., Ultrasmall Black Phosphorus Quantum Dots: Synthesis and Use as Photothermal Agents. *Angew. Chem. Int. Ed.* **2015,** *54*, 11526-11530.

(23) Robinson, J. T.; Tabakman, S. M.; Liang, Y.; Wang, H.; Sanchez Casalongue, H.; Vinh, D.; Dai, H., Ultrasmall Reduced Graphene Oxide with High Near-Infrared Absorbance for Photothermal Therapy. *J. Am. Chem. Soc.* **2011,** *133*, 6825-6831.

(24) Dai, S.; Li, T.; Wang, W.; Xiao, Y.; Lau, T.-K.; Li, Z.; Liu, K.; Lu, X.; Zhan, X., Enhancing the Performance of Polymer Solar Cells *via* Core Engineering of NIR-Absorbing Electron Acceptors. *Adv. Mater.* **2018,** *30*, 1706571.